Computers in Biology and Medicine 113 (2019) 103382

Contents lists available at ScienceDirect

Computers in Biology and Medicine

journal homepage: www.elsevier.com/locate/compbiomed

4D cardiac electromechanical activation imaging

Julien Grondin[a], Dafang Wang[b], Christopher S. Grubb[c], Natalia Trayanova[b], Elisa E. Konofagou[a,d,*]

[a] Department of Radiology, Columbia University, 630 W 168th, Street, New York, NY, 10032, USA
[b] Institute of Computational Medicine, Johns Hopkins University, Baltimore, MD, 21218, USA
[c] Department of Medicine, Columbia University, 630 W 168th, Street, New York, NY, 10032, USA
[d] Department of Biomedical Engineering, Columbia University, 1210 Amsterdam Avenue, New York, NY, 10027, USA

ARTICLE INFO

Keywords:
Cardiac activation mapping
Electromechanical wave imaging
3D ultrasound
3D activation mapping
Cardiac arrhythmia
High frame rate ultrasound

ABSTRACT

Cardiac abnormalities, a major cause of morbidity and mortality, affect millions of people worldwide. Despite the urgent clinical need for early diagnosis, there is currently no noninvasive technique that can infer to the electrical function of the whole heart in 3D and thereby localize abnormalities at the point of care. Here we present a new method for noninvasive 4D mapping of the cardiac electromechanical activity in a single heartbeat for heart disease characterization such as arrhythmia and infarction. Our novel technique captures the 3D activation wave of the heart in vivo using high volume-rate (500 volumes per second) ultrasound with a 32 × 32 matrix array. Electromechanical activation maps are first presented in a normal and infarcted cardiac model in silico and in canine heart during pacing and re-entrant ventricular tachycardia in vivo. Noninvasive 4D electromechanical activation mapping in a healthy volunteer and a heart failure patient are also determined. The technique described herein allows for direct, simultaneous and noninvasive visualization of electromechanical activation in 3D, which provides complementary information on myocardial viability and/or abnormality to clinical imaging.

1. Introduction

According to the latest report on Heart Disease and Stroke Statistics by the American Heart Association [1], more than 2300 Americans die of cardiovascular disease each day. Among the cardiovascular diseases, coronary artery disease (CAD) is by far the most deadly causing approximately 1 of every 7 deaths in the United States in 2015 [1].

Cardiac arrhythmias, such as atrial fibrillation and ventricular tachycardia, affect tens of millions of people worldwide [2,3] and can be associated with major causes of death such as stroke [4,5] and sudden cardiac arrest [6,7]. The disruption of the regular heart rhythm occurs in one or multiple regions of the heart, altering the normal propagation of electrical impulses [8]. Despite the need for efficiently diagnosing an increasing number of arrhythmia cases, there is currently no imaging technique available in the clinic that can noninvasively and reliably image the electrical and the electromechanical activities of the full heart. The current practice of cardiac electrical mapping involves introducing a catheter into the heart chambers to point-by-point map the endocardial surface with fluoroscopy guidance, often involving lengthy procedures [9]. An alternative non-invasive method, electrocardiographic imaging (ECGi), which, inferring epicardial potentials from body-surface potentials, has recently been developed [10,11]. However, this method is constrained to the epicardial surface and requires wearable electrode vests as well as constructing individualized torso/heart geometries from computed tomography (CT) scans. There is thus a severe lack of technology that can directly and noninvasively map the sequence of activation of the full heart in 3D. This would be critical in efficiently identifying and localizing arrhythmogenic regions for treatment planning and monitoring.

Here, we report 4D (3D over time) mapping of the electromechanical function of the heart to characterize heart disease, such as arrhythmia and infarction. Electromechanical Wave Imaging (EWI) can noninvasively map myocardial activation of the full heart in a single heartbeat throughout all four chambers in 4D. This technique images cardiac deformation resulting from electrical activation with high volume rates (500–2000 volumes per second) ultrasound to derive the electromechanical activation of the heart [12,13]. At the cellular level, it has been shown that action potential in a cardiac cell or myocyte is followed by cell shortening within tens of milliseconds [14]. The propagation of the onset of myocardial shortening in the heart can be described as an electromechanical wave, as it consists of mechanical deformations directly resulting from their local, respective electrical

* Corresponding author. Columbia University, 351 Engineering Terrace, MC 8904 1210, Amsterdam Avenue, New York, NY, 10027, USA.
E-mail addresses: jlg2216@columbia.edu (J. Grondin), ek2191@columbia.edu (E.E. Konofagou).

https://doi.org/10.1016/j.compbiomed.2019.103382
Received 3 May 2019; Received in revised form 30 July 2019; Accepted 4 August 2019

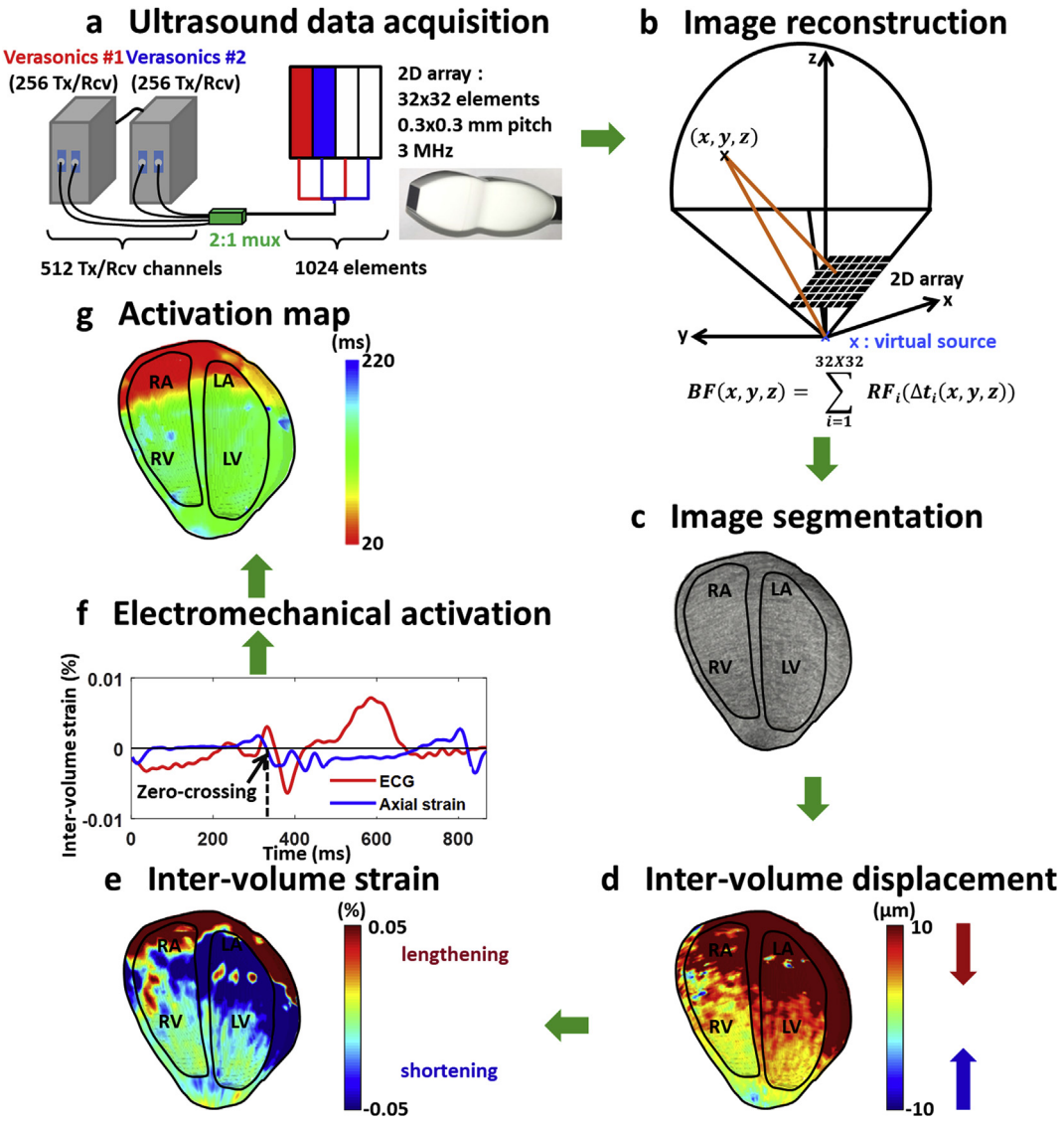

Fig. 1. Flowchart of 4D electromechanical wave imaging. Ultrasound data acquisition is performed with a 2D array connected to two Verasonics ultrasound scanners via a 2:1 multiplexer (a). High volume-rate imaging is performed with the transmission of a spherical wavefront and 3D image reconstruction is performed using a standard delay-and-sum method (b). The myocardium is manually segmented (c). Inter-volume axial displacements are estimated using 1-D normalized cross-correlation of the beamformed radiofrequency ultrasound signals (d). Positive displacements (red) indicate motion towards the transducer (at the apex) and negative displacements (blue) indicate motion away from the transducer. Inter-volume axial strains are estimated using a least-squares estimator (e). Positive strains (red) are associated with longitudinal lengthening and negative strains (blue) are associated with longitudinal shortening. Local onset of contraction is determined by the first positive to negative zero-crossing of the temporal axial strain curve after a reference time point, here the onset of the P wave (f). The electromechanical activation map is obtained by determining the onset of contraction in each voxel of the myocardium (g). LA: left atrium, RA: right atrium, RV: right ventricle, LV: left ventricle.

activations. Intrinsic or natural waves in the heart have been investigated for their relationship with myocardial function [15–17]. However, there are different types of waves in the heart. Our technique is referred to as electromechanical, rather than mechanical, wave imaging, since (1) it is different from a purely mechanical wave that is generated by the mitral or aortic valve closure [18], for instance, and (2) it is mapping the onset of myocardial shortening from inter-frame strain curves rather than peak strain obtained by speckle tracking echocardiography. An activation map as provided by EWI would strongly reflect cardiac electrical behavior, considering the strong correlation between electrical and EWI activation times demonstrated in previous in vivo [13,19,20] and in silico [21] studies. In a previous study, we have observed a decrease in both electromechanical activation times and QRS duration in patients responding to cardiac resynchronization therapy (CRT) [22]. More importantly, EWI could enable scientists to link the electrical and mechanical functions of the heart. Such linking capability is of high clinical value because cardiac diseases typically manifest themselves in both electrical and mechanical aspects, but is currently absent given the dearth of such mapping techniques in vivo. This technique uses transthoracic echocardiography and can be implemented in clinical ultrasound scanners. It has the potential of providing an early assessment of cardiac electromechanical function in care centers where echocardiography is available but not standard electrophysiology equipment and therefore inform the physician in order to improve pre-treatment planning.

While EWI does not provide a direct measurement of electrical activation, it results from the depolarization wave and therefore has great potential for cardiac activation and arrhythmia characterization. In a recent study, 2D EWI from four apical views were 3D-rendered and shown to be able to accurately predict the accessory pathways in Wolff-Parkinson-White syndrome pediatric patients [23]. However, cardiac activation is a dynamic 3D phenomenon and can originate between 2D

echocardiographic views. In addition, 3D rendering of multiple 2D views is not always suitable for patients with inconsistent heartbeat. Therefore, 4D ultrasound is needed to capture the electromechanical activation of the full heart. Cardiac electromechanical imaging has recently been shown with 3D ultrasound, but in isolated Langendorff-perfused pig and rabbit hearts [24]. The performance of 4D ultrasound for imaging the electromechanical wave and investigating its relationship with electrical activation can well be studied in silico as it provides a point-by-point comparison. In a previous study, we investigated the relationship between electrical and electromechanical activation in an infarct-free canine heart model [21]. In this study, we are using a post-myocardial infarct patient-specific as well as an infarct-free human heart model. In addition, in the previous study, the comparison between electrical and electromechanical activation times was performed in 2D cross-sections of the heart, while in this study, the comparison is performed in the full 3D volume of the ventricles. Also, the simulated electromechanical activation times were directly obtained from finite-element simulated strain, while in this study, the simulated electromechanical activation times are obtained from simulated 3D ultrasound imaging of the heart model. This is of key importance, as the characteristics of the ultrasound transducer can affect its spatial resolution and, therefore, the accuracy of the strain estimation.

In this proof-of-concept study, we aim at demonstrating that 4D high volume-rate ultrasound can image the propagation of the electromechanical wave and provide electromechanical activation maps. First, the feasibility of 4D EWI is shown in silico in an infarct-free and an infarcted ventricule. Then, we demonstrate 4D EWI in vivo in a canine model during sinus rhythm, ventricular pacing and ventricular tachycardia (VT), and in vivo in a human during normal sinus rhythm and in a heart failure patient during right ventricular and biventricular pacing.

2. Methods

2.1. Ultrasound system configuration

4D EWI was performed using volumetric ultrasound imaging with a 2D array of 32 × 32 transducers elements, with an inter-element spacing (or pitch) of 0.3 mm and a center frequency of 3 MHz (Vermon SA, France) (Fig. 1). The 2D array, which has a total of 1024 transducer elements, was connected to two identical ultrasound scanners (Vantage, Verasonics, Kirkland, WA), each of which having 256 transmit/receive channels. In order to use all the elements of the 2D array, a 2:1 multiplexer, allowing for switching from one half of the array to the other half was used. In a later phase of development of the ultrasound system, the 32 × 32 array was connected to four synchronized Verasonics ultrasound scanners, without multiplexer, in order to have a 1:1 element to pin mapping. This allows for more custom programing of imaging sequence and higher temporal resolution between reconstructed images. We designed our ultrasound acquisition system to achieve a spatial resolution on the order of a few millimeters and a temporal resolution of 2 ms to capture the electromechanical wave. In the simulation study, a 3D electromechanical heart model was created and ultrasound imaging of the electromechanical wave was performed with a simulated ultrasound transducer with the aforementioned characteristics. Then, we performed 4D EWI in vivo with a system of either 2 or 4 ultrasound scanners.

2.2. Computer simulation of heart function

An electromechanical heart model was used in conjunction with a 3D ultrasound simulation program to demonstrate the feasibility of 4D EWI. Our electromechanical finite-element heart model consists of two coupled parts, an electrophysiological model and a mechanical model. The electrophysiological component represents the activation and propagation of cardiac action potentials by solving a reaction-diffusion partial differential equation. The mechanical component describes the heart deformation by the balance-of-force equation in which the active contraction force of myofilaments drives the cyclic heart motion; myocardial tissue was regarded as an orthotropic, hyperelastic, and nearly-incompressible material. The electrophysiological and mechanical models were coupled at the cellular level: the membrane ionic kinetics regulates the intracellular calcium transient, which provides the trigger for myofilament contraction. The ionic model of cellular action potential, here a human ionic model [25], was coupled to the Rice et al. myofilament model [26] adapted to human mechanics [27]. The electromechanical model has been developed and validated in a number of previous publications [28–31], where full detail regarding boundary conditions, numerical approaches and parameter values is provided. Verification of the software (Hopkins-MESCAL) and benchmarking of its performance against other electromechanical simulators has been conducted in a previous study [32].

The electromechanical simulations here were executed on geometrical models reconstructed from MRI images. Simulations were performed only in the ventricles due to the limited resolution of MRI and the complexity of fiber orientation in the atria. While we have previously constructed MRI-based electromechanical models of ex-vivo hearts and used them in a number of publications [27,33–37], this is the first time we use clinical, contrast-enhanced (late gadolinium enhanced, LGE)-MRI scans of patient hearts, making it possible to represent structural remodeling associated with myocardial infarction (MI). Post-MI patient-specific models have been previously used by our team for electrophysiological simulations [38,39], but not for electromechanical. Segmentation of LGE-MRI and geometrical model construction, including assigning fiber orientations in the models using a rule-based approach [40], has been described in full detail in these previous publications [38,39,41]. For this study we used one of the post-MI patient-specific heart models utilized in our recent study [39]. We simulated the deformation of this post-MI patient heart during sinus rhythm. The infarct region was modeled as electrically non-conductive, with no active contraction force and 5-times stiffer than normal tissue. A small infarct border zone, with intermediate properties between normal and scar tissue, was modeled surrounding the infarct. For a control simulation, the infarct region was removed and the simulations repeated. Electrical activation time was defined as the time of maximum temporal derivative of electrical potential. As a baseline value, the duration of the simulated heartbeat was assumed to be 1000 ms.

Once the electromechanical simulations were completed, the ultrasound simulation program Field II [42–44] was used to generate the ultrasound radio-frequency channel signals with a simulated transducer and a distribution of point scatterers modeling the tissue. Field II uses the Tupholme [45] and Stepanishen [46] method based on spatial impulse response for calculating pulsed ultrasound fields. It can be used for all purpose anatomical and functional ultrasound imaging as shown in previous literature [47–51]. In our study, the scatterers were uniformly distributed at random positions in the ventricles, which geometry and displacement were obtained from the mechanical finite-element simulation at each time step. Electronic noise was not simulated. High volume-rate imaging was achieved by using diverging wave imaging [52,53]. Ultrasound diverging wave imaging consists in transmitting an ultrasound wave which wave front widens (or diverges) as the wave propagates from the transducer to the tissue. This was achieved by placing a virtual source 4.8 mm behind the surface of the transducer, which generated a spherical wave front (the set of points where the wave has the same phase) with a transmit angle field of view of 90°. This allows for reconstructing the entire image from a single transmitted wave using parallel beamforming, which means that all the lines that form the ultrasound image are reconstructed from the signals received from the same transmitted wave. A standard delay-and-sum algorithm, implemented on a GPU (Tesla K40c, NVIDIA, Santa Clara, CA), was used to reconstruct the image in a pyramidal scan format, with an axial sampling of 32.1 μm, a sector angle of 90° and a density of one

line per degree in both lateral and elevational directions. The beamformed data *BF* at a given location *(x, y, z)* of the reconstructed volume is given by:

$$BF(x, y, z) = \sum_{i=1}^{1024} RF_i(\Delta t_i(x, y, z)) \quad (1)$$

where RF_i is the RF signal received on transducer element i and $\Delta t_i(x,y,z)$ is sum of the forward delay from the transducer to *(x,y,z)* and the backward delay from *(x,y,z)* to transducer element *i*. The displacement obtained from the mechanical finite-element simulation was 3D linearly interpolated onto the position of the scatterers, which were displaced accordingly at each time step. The ventricles were imaged at each time step (1.8 ms) during an entire heartbeat, which entails an imaging rate of 556 vol per second.

2.3. Animal protocol

The canine study complied with the Public Health Service Policy on Humane Care and Use of Laboratory Animals and was approved by the Institutional Animal Care and Use Committee of Columbia University. Four male mongrel canines (24.1 ± 1.0 kg) were premedicated with diazepam (0.2–1 mg/kg) injected intravenously and then anesthetized with an intravenous injection of propofol (2–5 mg/kg). The canines were mechanically ventilated with a rate- and volume-regulated ventilator on a mixture of oxygen and titrated 0.5–5% isoflurane. Lidocaine (30–50 μg/(kg.min)) was injected intravenously throughout the procedure and until the end of the experiment to minimize the occurrence of ventricular arrhythmia. A left lateral thoracotomy was performed with electrocautery and one or two ribs were removed to expose the heart. In the first two canines, no other procedures were performed before ultrasound data acquisition during normal sinus rhythm. In the third canine, one external bipolar electrode was sutured onto the epicardial surface of the LV in the vicinity of the apical region. The epicardial electrode was connected to a function generator (AFG3022C, Tektronix, Beaverton, OR), delivering a 1-V amplitude, 2-ms pulse width at a period of 400 ms. In the fourth canine, the proximal left anterior descending (LAD) artery was ligated [54] to create a myocardial infarct. The thoracotomy incision was then repaired in layers and the skin closed with surgical staples. The canine was maintained during 3 days in post-operative care during the development of the infarct. Afterwards, the chest was re-opened following the same procedure as described earlier, and ultrasound and electrical data acquisition were performed during sinus rhythm and during ventricular tachycardia (VT). In order to induce VT, lidocaine injection was stopped and pacing was performed with one electrode positioned (not sutured) on the epicardial surface near the infarct border zone. The pacing signal amplitude and pulse width were similar as described above. The pacing signal period was initially set to 400 ms. Pacing was performed for 10–15 s. After the pacing was turned off, if the canine was maintained in VT, ultrasound and electrical mapping were performed. If the canine reverted to sinus rhythm, the pacing electrode was moved to a different location and pacing was resumed. The pacing signal period was decreased by step of 20 ms if VT was not induced after trying various pacing locations.

Electroanatomical mapping of the ventricular surface was performed using a bipolar catheter (TactiCath, St. Jude Medical, Saint Paul, MN). The 3D position of the catheter was obtained from a navigation system (EnSite Precision, St. Jude Medical, Saint Paul, MN) using adhesive sensor patches placed on the canine. The time corresponding to the maximum of the electrograms at a given location was defined as the electrical activation time. An epicardial electrical activation map was generated and anatomical landmarks were added for co-registration with EWI mapping.

2.4. In vivo ultrasound acquisition

Ultrasound imaging was performed during normal sinus rhythm, epicardial pacing and ventricular tachycardia in the open-chest canines and transthoracically during normal sinus rhythm in a healthy human volunteer and during right ventricular and biventricular pacing in a heart failure patient. The human study protocol was approved by the Institutional Review Board of Columbia University and is in accordance with its ethical standards. Informed consent was obtained from the participants.

Both diverging and conventionally focused wave imaging sequences were used to image the canine heart. The ultrasound probe was positioned to acquire apical views of the heart. For diverging wave imaging, similarly to the ultrasound simulations, a virtual source was placed 4.8 mm behind the surface of the transducer to allow for high volume-rate imaging. In the two-ultrasound scanner configuration, the first and the second halves of the 2D array aperture (or active area) were used alternatively for each transmit-receive event at a pulse repetition frequency of 1000 Hz. Two consecutive transmit-receive events using each half of the aperture were used to reconstruct an entire image, yielding an imaging rate of 500 volumes per second. In the four-ultrasound scanner configuration, all the elements of the 2D array were used simultaneously for diverging wave imaging. This later version of our ultrasound system was used to perform 3D EWI in a single canine using single diverging wave imaging at 600 volumes per second. For both systems configuration, the ultrasound channel data were acquired during 2 s. GPU-accelerated delay-and-sum beamforming, identical to the one used in the simulation, was performed.

2.5. Electromechanical wave imaging of the heart

Normalized cross-correlation [55] (5 mm window, 70% overlap) of beamformed RF signals in the axial direction was used to estimate inter-volumes displacements. Axial displacements were low-pass filtered in time with a cut-off frequency of 125 Hz. The axial inter-volume strains were obtained using a least-squares estimator implemented with a Savitzky-Golay filter [56]. The axial inter-volume strains were mapped to a volume of 256 × 256 × 256 voxels. For the computer simulations, the Pearson correlation coefficient as well as the median relative difference (MRD) between estimated and ground truth inter-volume axial strains were computed across all voxels and all time points, totaling $N = 3.2*10^6$ comparison points.

For in vivo imaging, segmentation was performed from focused 2D ultrasound images acquired immediately after the diverging wave imaging sequence for the two ultrasound systems configuration and from focused 3D ultrasound images for the four ultrasound systems configuration. For the two systems configuration, focused 2D image acquisitions were performed using one quarter of the 2D array aperture (32 × 8) and by steering the focused beam in the lateral direction over a 90° sector angle with a beam density of one line per degree while the elevational focus was set to a depth of 70 mm. The epicardial and endocardial contours as well as the atrial and ventricular septum were manually segmented from the 2D ultrasound image. The segmentation in the elevational direction was performed by assuming central symmetry of the left atria and ventricle and of the epicardial and endocardial contours at each depth (Fig. 2). For the four systems configuration, focused 3D image acquisitions were performed using the full 2D array aperture and by steering the focused beam in the lateral and elevational direction over a 90° sector angle with a beam density of one line per degree. The epicardial and endocardial contours as well as the atrial and ventricular septum were manually segmented from the 3D ultrasound image for each transverse slice of the reconstructed 3D volume. By positioning the ultrasound transducer to acquire apical views, the direction of propagation of the ultrasound beam (or axial direction) was approximately aligned with the longitudinal direction of the heart. Therefore, myocardial contraction, which is associated with

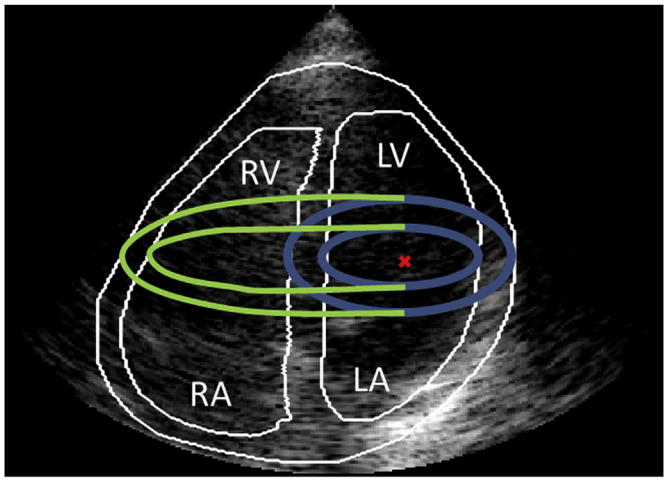

Fig. 2. Illustration of the segmentation in the elevational direction. The myocardium is first segmented from a 2D B-mode (delineation in white color). Then, for every depth, the center of the left side of the heart (ventricle or atria) is determined (red cross). Elevational segmentation is performed by assuming circular shape (blue circles) of the left ventricle (LV) and ellipsoidal shape (green ellipsoid) of the right ventricle (RV). LA: left atrium, RA: right atrium.

longitudinal shortening, corresponded to negative axial strain. The onset of longitudinal shortening, resulting from electrical activation, was determined by the time of first positive-to-negative zero-crossing of the axial strain curves after a reference time point and was defined as the electromechanical activation time.

2.6. Semi-automated detection of activation times

In previous 2D EWI studies, pixels were manually selected from the myocardium and the zero-crossing corresponding to the activation time were manually selected. Given the large number of voxels in 3D EWI and in order to minimize potential bias in the detection of activation times, this process was semi-automated. For each voxel in of the reconstructed myocardial volume, the electromechanical activation time was semi-automatically computed. During normal sinus rhythm, the reference time point was set to the onset of the P-wave for voxels located in the atria and to the onset of the QRS complex for voxels located in the ventricles. During ventricular pacing, the reference time point was set to the time of pacing. The reference time point was manually selected from the ECG trace and the atrio-ventricular junction was manually selected from the ultrasound B-mode. In the atria, a search time window starting from the onset of the reference time point to the onset of the Q-wave was defined, while in the ventricle a search time window of approximately 200–300 ms starting from the reference time point was defined to look for zero-crossings occurrences. All positive to negative zero-crossings were automatically detected in the search time window. Multiple zero-crossings can occur within the search time window, with occasionally low strain magnitude after crossing and a negative to positive zero-crossing following immediately or soon after. This may not be related to a physiological electromechanical activation. The zero-crossing corresponding to the electromechanical activation time, at a given voxel, was defined as the first positive to negative zero-crossing within the search time window, for which, the inter-volume axial strain curve was consistently positive and with a mean value above a threshold Th_{strain}, 5 ms before the zero-crossing and consistently negative and with an absolute mean value above the threshold Th_{strain}, 5 ms after the zero-crossing. In this study, Th_{strain}, ranging between 0.0001% and 0.05%, and the 5 ms time window were manually and empirically selected from previous experience with manual selection of zero-crossings for EWI. The threshold Th_{strain} was kept constant for a given 3D EWI activation map. The performance of the semi-automated detection of activation time was evaluated against manual detection performed by an operator blinded to the semi-automated detection results. The Pearson correlation coefficient was computed between semi-automatically and manually detected activation times. A 3D linear interpolation was performed for voxels where no zero-crossing meeting the aforementioned criteria was found, in order to obtain the electromechanical activation map or isochrone.

2.7. Comparison between electrical and EWI mapping

The 3D coordinates and electrical activation times were extracted from the electroanatomical mapping system for apical pacing and VT. However, the electrical data during sinus rhythm of the infarcted canine were not correctly saved and could not be retrieved after generation of the electrical map. Both electrical and EWI maps were imported in the open-source 3D visualization software Paraview (Paraview v5.6, www.paraview.org). The electroanatomical and EWI maps were manually co-registered and aligned using anatomical landmarks such as anterior and lateral regions of the LV at the basal and mid-level, the LV and RV apex. Anatomical landmarks were labelled onto the electroanatomical map during electrical mapping by the operator, who could directly visualize the heart and tip of the mapping catheter. After alignment of both maps, the catheter recording locations were matched with the closest voxels on the epicardial surface of the EWI activation map. Linear regression between EWI and electrical activation times was performed and the Pearson correlation coefficient was calculated. The median relative difference between electrical and electromechanical activation times was also computed. All data processing and analyses was performed with Matlab R2017a (MathWorks, Natick, MA).

2.8. Lateral resolution assessment

The lateral resolution of the 32 × 32 array using the 2 systems and 4 systems configuration was evaluated and compared to that of a 1-D array at 2.5 MHz center frequency with a 20.5 mm aperture (ATL, P4-2) used in previous EWI studies. The probe was positioned on the surface of a commercial ultrasound phantom (84–317, Fluke Biomedical, Everett, WA) and the full width half maximum of the lateral profile of a point target located at a depth of 40 mm was measured. Two diverging waves was used with the two-system configuration in order to use the full aperture, while single diverging wave imaging was used for the 4 systems configuration and the 1-D array.

3. Results

4D, high-volume-rate EWI was capable of mapping the electromechanical activation of the entire heart noninvasively and in a single heartbeat. The heart was imaged in the apical view with 4D ultrasound using emission of diverging acoustic waves to achieve high volume-rate imaging. Inter-volume axial, i.e. along the ultrasound beam or approximately apex-to-base, displacements and strains were subsequently estimated and the local onset of myocardial contraction was derived. The electromechanical activation map was then obtained by determining the local onset of contraction for each voxel of the myocardium. Anterior views of the heart are consistently shown in the figures. When comparing EWI and electrical mapping, the figures show approximately a projection of the epicardial surface of the anterior region of the ventricles, since this was the main reachable region for electrical mapping. During sinus rhythm mapping, the figures show a longitudinal cutting plane of the myocardium, in order to better visualize the propagation of the electromechanical ventricles in all four chambers. The supplementary movies show different projections of EWI mapping to fully visualize the activation.

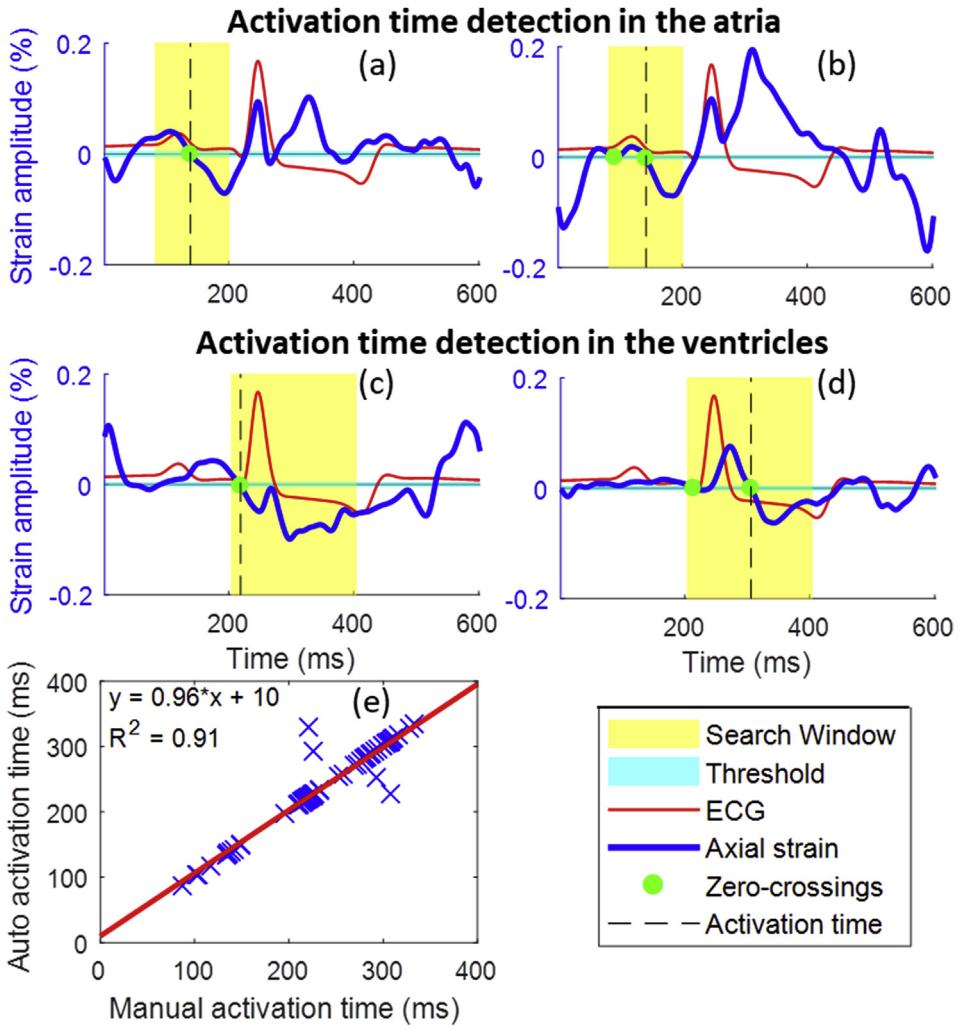

Fig. 3. Automatic detection of positive to negative zero-crossings (green dot) and electromechanical activation times (black dotted line) in a healthy canine heart. Examples of inter-volume axial strain curves and activation time detection at a given location in the atria (a,b) and the ventricles (c,d). The first significant positive to negative zero-crossing in the search window is defined as to the electromechanical activation time. Semi-automatically and manually detected activation times were well correlated (e).

3.1. Electromechanical activation time detection

Examples of semi-automated detection of the electromechanical activation time are shown in the atria (Fig. 3a and b) and in the ventricle (Fig. 3c and d). Inter-volume axial strain curves (in blue color) for a given voxel location are shown as a function of time and the ECG (in red color) is shown as well. Unambiguous activation detection can be found, such as shown in Fig. 3a and c with a single zero-crossing with significantly (above threshold) high positive magnitude before crossing and negative magnitude after crossing. Multiple zero-crossing can also be found in the search window, as shown in Fig. 3b and d. In these cases, the algorithm selected the second zero-crossing, since the first one was not significant, which is consistent with what an operator would have chosen manually. As shown by Fig. 3e, semi-automatically detected activation times were well correlated with manually detected activation times (R^2 = 0.91, slope = 0.96, intercept = 10 ms).

3.2. In silico EWI of human hearts

To demonstrate the feasibility of 4D EWI, an ultrasound simulation program (Field II [44]) was used in combination with finite-element electromechanical simulation of a human heart model reconstructed from MRI images [31]. The electrophysiological model represents the activation and propagation of cardiac action potentials by using a reaction-diffusion partial differential equation. The heartbeat was then imaged with 4D ultrasound at 556 volumes per second. Inter-volume axial displacements and strains were estimated from the ultrasound radiofrequency (RF) signals. Ventricular axial strains estimated with ultrasound were compared to their computational equivalents in the infarct-free and infarcted hearts (Fig. 4, Supplementary Movies 1-5).

Supplementary video related to this article can be found at https://doi.org/10.1016/j.compbiomed.2019.103382.

Snapshots at different time points after the onset of electrical activation illustrate the propagation of the electromechanical wave. Negative strains, indicating shortening, are in blue color and correspond to myocardial contraction. In the simulated infarct-free heart, early contraction occurs in the ventricular septum, between the right and left ventricles, as well as in the anterior basal region of the right ventricle (Fig. 4a). Myocardial contraction then propagates in both ventricles. Snapshots of the estimated axial strains (Fig. 4c) were in good agreement with their true counterparts (Fig. 4a) as they exhibit a similar pattern. The correlation coefficient and the median relative difference between true and estimated strains were R^2 = 0.93, MRD = 49.6%. True electrical activation times (Fig. 4b) were also in good agreement with the estimated electromechanical activation times (Fig. 4d). The electrical activation maps, or isochrones, exhibited early

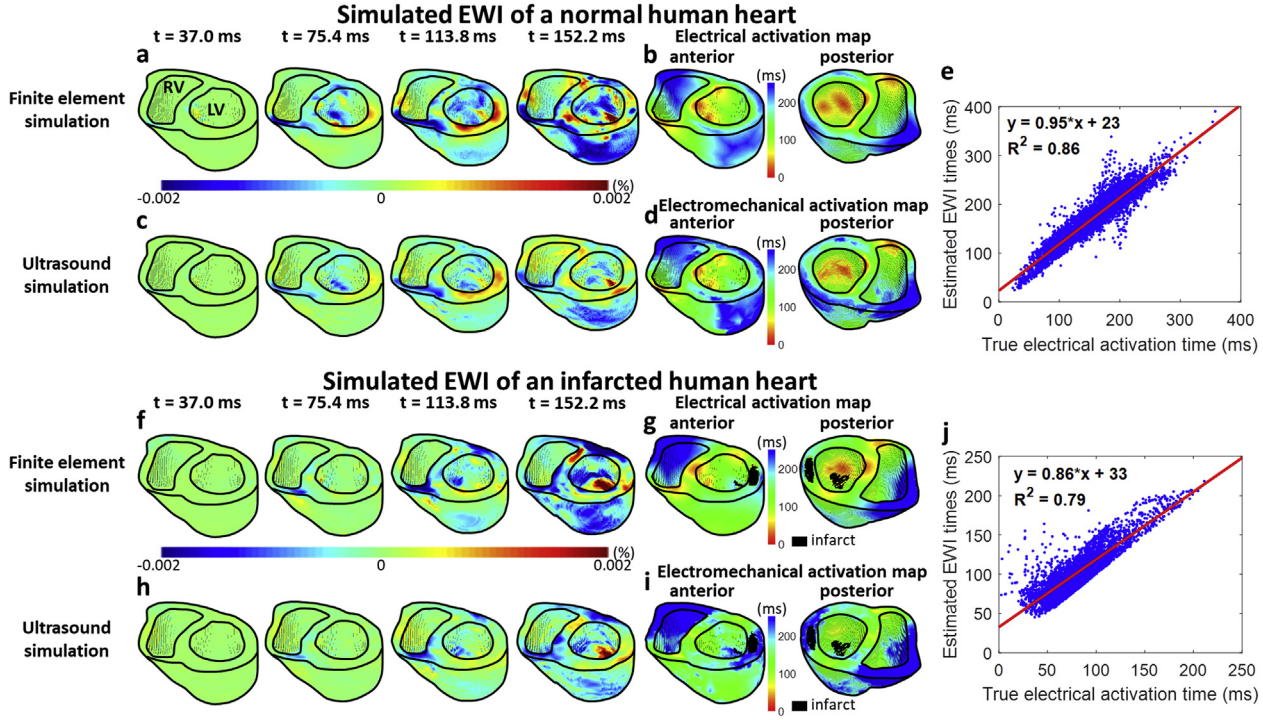

Fig. 4. Simulated electromechanical wave imaging. Snapshots of the axial strain obtained from benchmark mechanical finite-element simulation in the infarct-free baseline (a) and infarcted (f) hearts and estimated from high frame-rate 4D ultrasound simulation in the infarct-free (c) and infarcted (h) hearts, in the right (RV) and left (LV) ventricles at different time points are shown. The electrical activation times obtained from the electromechanical model in the infarct-free (b) and infarcted (g) hearts as well as the electromechanical activation times obtained from the ultrasound simulation in the infarct-free (d) and infarcted (i) hearts are shown. Good agreement was found between benchmark electrical activation times and estimated electromechanical activation times in both the infarct-free (e) and the infarcted (j) heart models. Infarcted regions (in black), located in the lateral LV and at the apex of the anterior LV were not activated.

activation (in red) in the septal region, the endocardial layer of the anterior left ventricle (LV), the anterior region at the base of the right ventricle (RV) and the posterior-septal region at the base of the LV. The electromechanical activation map obtained from EWI also highlights these regions as earliest sites of activation. Late sites of activation were found in the posterior region of the RV at the basal level, in the epicardial layer of the anterior-lateral region of the LV and in the basal region of the posterior-lateral LV. A strong correlation ($R^2 = 0.86$, N = 452,715 points, Fig. 4e) was obtained between true electrical (Fig. 4b) and estimated (Fig. 4d) EWI activation times.

In the infarcted heart, we also found a similar pattern of electromechanical wave propagation for the benchmark (Fig. 4f) and the estimated (Fig. 4h) axial strains. The correlation coefficient and the median relative difference between true and estimated strain were $R^2 = 0.96$ and MRD = 32.4%, respectively. Good agreement ($R^2 = 0.79$, N = 370,295 points, Fig. 4j) was obtained between the true electrical (Fig. 4g) and the estimated electromechanical (Fig. 4i) activation times and the median relative difference was 23.3%. The infarct region was not sufficiently activated.

3.3. *In vivo EWI of a canine during sinus rhythm*

We assessed the in vivo feasibility of 4D EWI and cardiac activation mapping in a canine model using two synchronized ultrasound scanners and a multiplexer (Fig. 5a and b) and four synchronized ultrasound scanners (Fig. 5c and d). Inter-volume axial strains were imaged during a single heartbeat (Supplementary Movie 6 and 8). EWI images of the inter-volume axial strains across all chambers in the heart at different time points of the cardiac cycle show the propagation of the electromechanical wave (Fig. 5a and c). The earliest myocardial contraction (in blue) occurs in the right atrium (RA), during the P-wave. The electromechanical wave then propagates to the left atrium (LA). After the onset of the QRS complex, early contraction occurs in the ventricular septum and then propagates to both ventricles. The presence of multiple locations of Purkinje-ventricle junction causes a complex activation pattern during normal sinus rhythm. The propagation of the electromechanical wave is consistent with the ECG, which is a purely electrical measurement of cardiac activity. The electromechanical activation times were mapped onto the canine heart (Fig. 5b and d and Supplementary Movie 7 and 9) where early activation times are in red and late activation times are in blue. The electromechanical activation map obtained with EWI is consistent with the ECG and the known sequence of electrical activation of a normal heart [57].

Supplementary video related to this article can be found at https://doi.org/10.1016/j.compbiomed.2019.103382

3.4. *In vivo EWI of a canine during electrical pacing*

Validation of electromechanical mapping was also performed in a canine in vivo against electroanatomical mapping. One pacing electrode was sutured onto the epicardial surface of the heart in the anterior region of the LV near the apex (Fig. 6f). During apical pacing, both ventricles were imaged with high-volume rate 4D ultrasound in a single heartbeat. The earliest region of contraction (in blue) was found in the apical region (Fig. 6a), near the position of the pacing electrode. Then, the electromechanical wave propagated towards the base in both ventricles (Fig. 6b–e and Supplementary Movie 10). Isochronal maps obtained from EWI (Fig. 6g and Supplementary Movie 11) and from electroanatomical mapping (Fig. 6h) are shown. The earliest regions (in red) of electromechanical and electrical activations are located in the apical region, near where the electrode was pacing from (Fig. 6f). Relatively good agreement ($R^2 = 0.58$, slope = 0.9, intercept = 21 ms, N = 20 points) was found between EWI and electrical mapping (Fig. 6i). The basal level of the LV was not taken into consideration in the correlation analysis since no electrical data were available in this

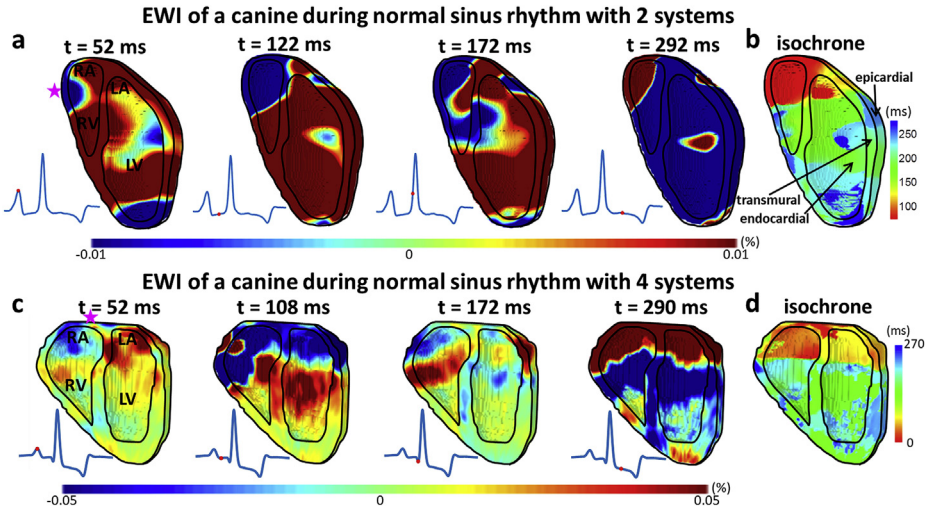

Fig. 5. In vivo electromechanical wave imaging during normal sinus rhythm in a canine using 2 ultrasound scanners and a multiplexer (a,b) and in another canine using 4 ultrasound scanners without multiplexer (c,d). Snapshots of the axial strain obtained from 4D high volume-rate ultrasound imaging at different time points (a,c) are shown. The ECG is also shown, with the corresponding time point indicated by a red dot. The electromechanical activation times of the heart are shown (b,d). In both cases, the earliest activation starts in the right atrium (RA), then propagates to the left atrium (LA), and finally to left (LV) and right (RV) ventricles via the interventricular septum. Examples of epicardial, transmural and endocardial regions are indicated with a black arrow (b) to assist with 3D visualization.★: earliest site of activation.

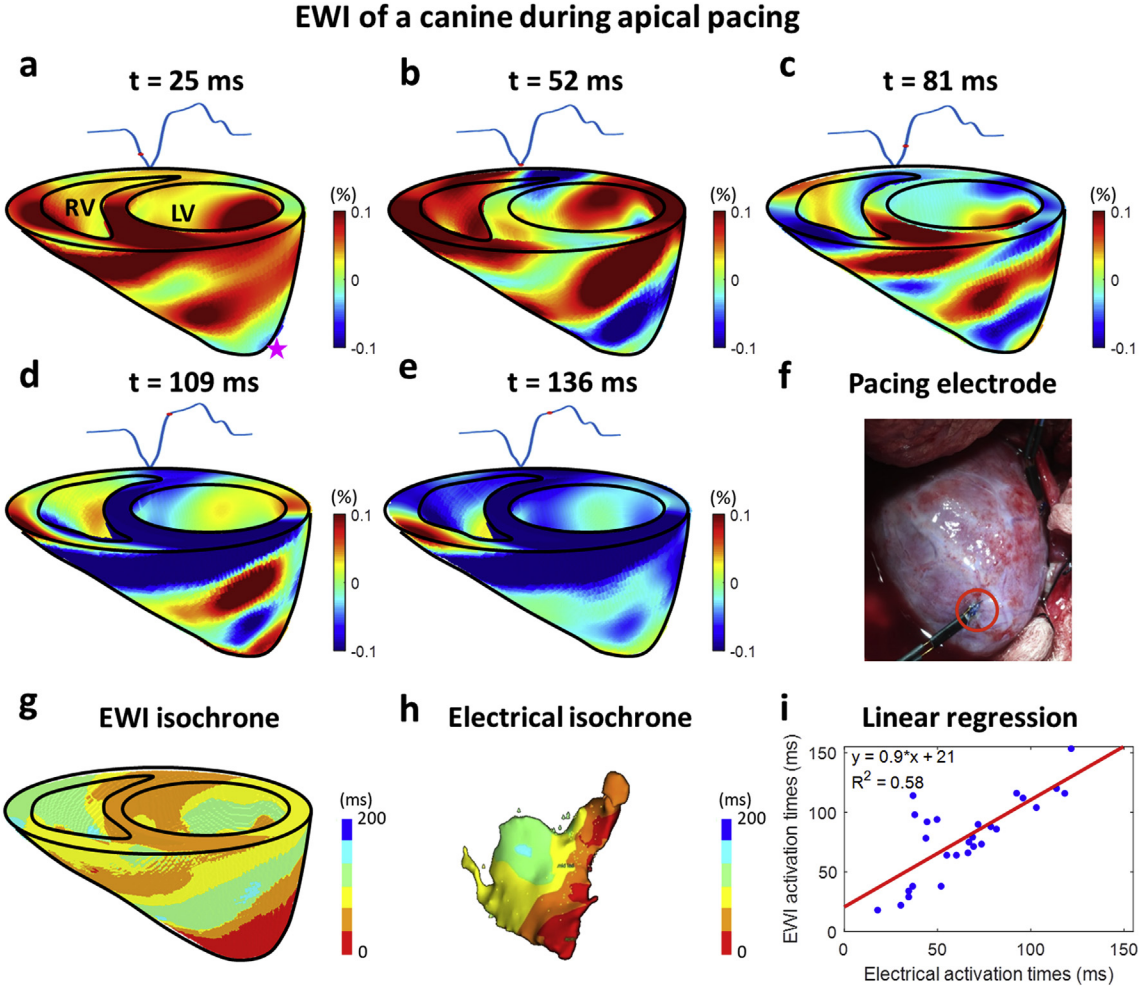

Fig. 6. In vivo electromechanical wave imaging of a canine during apical pacing. Snapshots of the axial strain obtained from 4D high volume-rate ultrasound imaging at different time points (a–e) are shown. The ECG is also shown, with the corresponding time point indicated by a red dot. A picture of the heart, with the pacing electrode inside the red circle is shown (f). The electromechanical activation times of the heart is shown (g). The electrical activation map of the epicardium obtained from electro-anatomical mapping (h) is in good agreement with the EWI map (i). The earliest activation is in the apical region of the heart, near where the electrode is pacing from. RV: right ventricle, LV: left ventricle, ★: earliest site of activation.

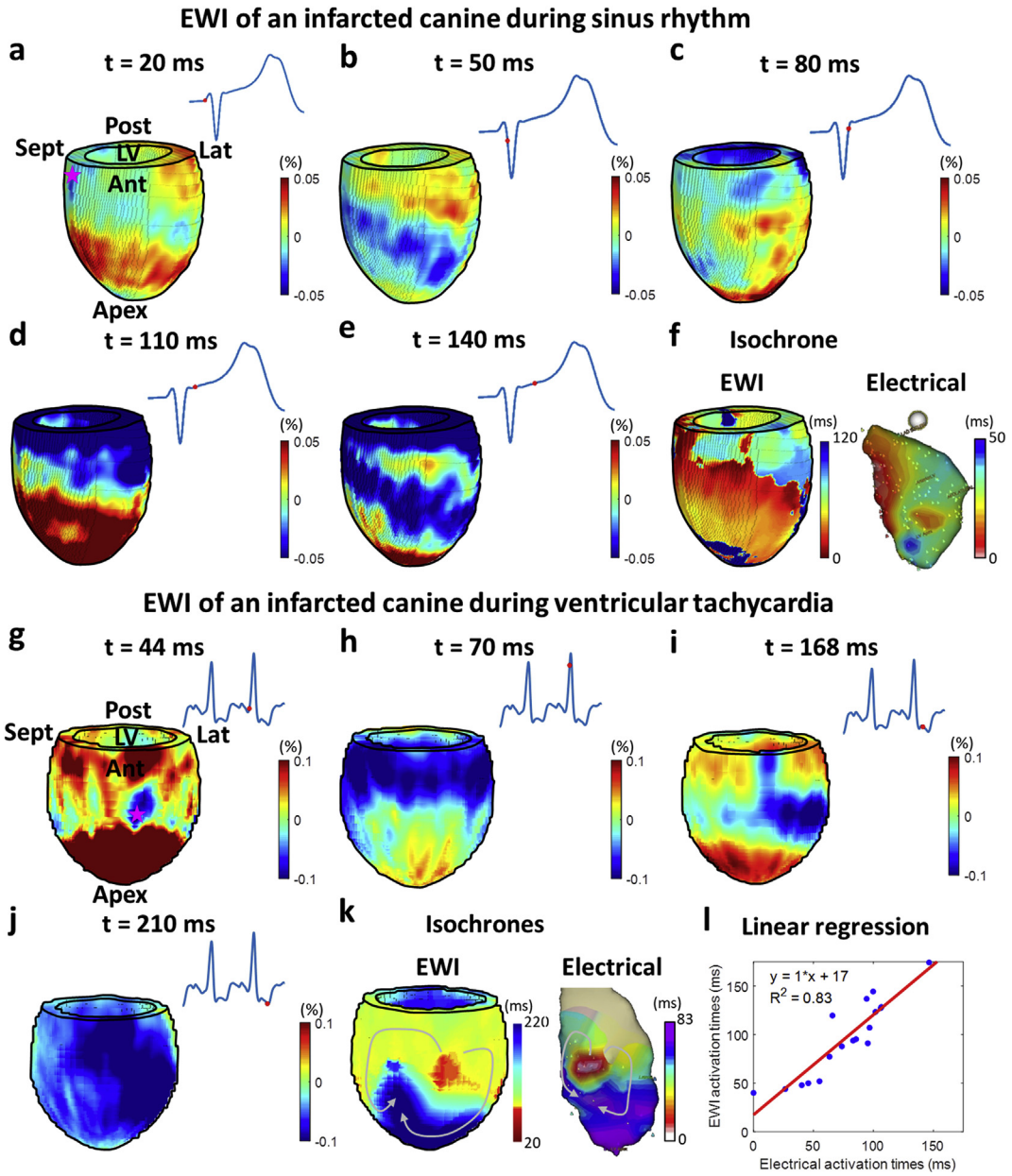

Fig. 7. In vivo electromechanical wave imaging of an infarcted canine during sinus rhythm (SR) and during ventricular tachycardia (VT). Snapshots of the left ventricular (LV) axial strain obtained from 4D high volume-rate ultrasound imaging at different time points (a-e for SR and g-j for VT) are shown. The ECG is also shown, with the corresponding time point indicated by a red dot. The electrical and electromechanical activation times of the LV are in good agreement (f for SR and k-l for VT). For SR, early activation is observed at the basal level of the anterior-septal and mid-level of the anterior area. For VT, early activation was observed at the mid-level of the anterior region and late activation was observed in the anterior-septal area between apical and mid-level, adjacent to the early activated region. The arrows in gray color indicate the activation propagation and suggest the presence of a re-entry loop in that area. ★: earliest site of activation.

region.

Supplementary video related to this article can be found at https://doi.org/10.1016/j.compbiomed.2019.103382.

3.5. In vivo EWI of an infarcted canine during sinus rhythm and VT

Validation of electromechanical mapping was also performed in an infarcted canine in vivo during sinus rhythm and during VT. Myocardial infarct was obtained after left anterior descending artery ligation and developed during 3 days. The infarcted region was found to be in the anterior LV, extending from apical to mid-level. VT was induced after pacing the epicardial surface for 10–15 s in the infarct border zone, approximately in the anterior region at the mid-level. High-volume rate single-heartbeat 4D ultrasound and electroanatomical mapping were performed similarly as described above. During sinus rhythm, the earliest region of contraction (in blue) was found at the base of the anteroseptal region (Fig. 7a) and the latest activated region was found at the apex. The propagation of the electromechanical wave was imaged (Fig. 7a–e and Supplementary Movie 12) and the electromechanical and electrical activation times were found to be in good agreement, showing similar early and late activated regions (Fig. 7f and Supplementary Movie 13).

Supplementary video related to this article can be found at https://doi.org/10.1016/j.compbiomed.2019.103382.

During VT, while the ECG trace is not a typical VT morphology (Fig. 7g–j), the simultaneous onset of tachycardia (not shown in Fig. 7), reversal of QRS axis and widening of QRS (although still not as wide as in typical VT) highly suggest a ventricular rhythm. Only one VT map

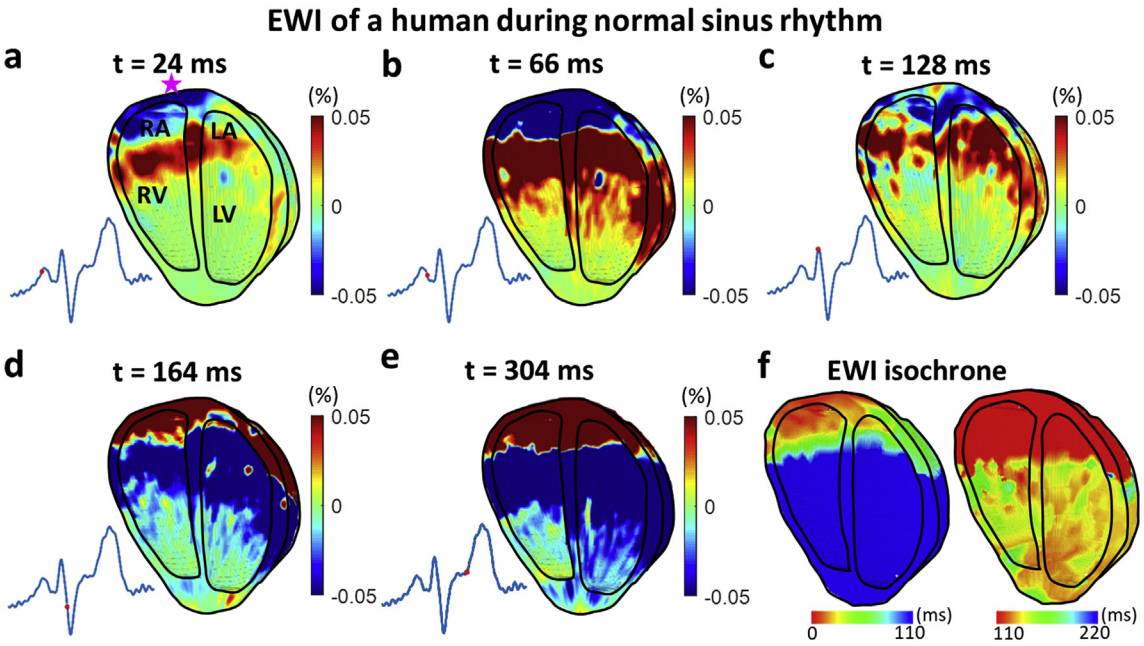

Fig. 8. In vivo electromechanical wave imaging of a human volunteer during normal sinus rhythm. Snapshots of the axial strain obtained from 4D high volume-rate ultrasound imaging at different time points (a–e) are shown. The ECG is also shown, with the corresponding time point indicated by a red dot. The electromechanical activation times of the heart is shown with two different time scale to better visualize atrial and ventricular activation separately (f).The earliest site of activation is observed near the sinus node in the right atrium (RA). The electromechanical wave then propagates to the left atrium (LA) (b) and finally to both ventricles (c–e). The isochrone shows a typical cardiac activation map during normal sinus rhythm. RV: right ventricle, LV: left ventricle, ★: earliest site of activation.

was generated. The earliest region of contraction (in blue) was found at the mid-level of the anterior region (Fig. 7g) and the latest activated region was located adjacently, in the antero-septal area between the apical and mid-level. The propagation of the electromechanical wave was imaged during VT (Fig. 7g–j and Supplementary Movie 14) and the electromechanical and electrical activation times were also found to be in good agreement (R^2 = 0.83, slope = 1.0, intercept = 17 ms, N = 18 points) (Fig. 7l and Supplementary Movie 15). The gradation in conduction timings as well as the short anatomic distance between early and late activation times highly indicates the presence of a re-entry rather than a focal mechanism associated with the VT.

Supplementary video related to this article can be found at https://doi.org/10.1016/j.compbiomed.2019.103382.

3.6. In vivo EWI of a normal human heart

The feasibility of noninvasive 4D activation mapping of the human heart in a single heartbeat using EWI was performed in a healthy 26-year old volunteer during normal sinus rhythm. High volume-rate ultrasound imaging was performed transthoracically and the ECG was acquired simultaneously. EWI images show early contraction in the RA, followed by the LA and then in both ventricles (Supplementary Movie 16, Fig. 8a–e). The electromechanical activation map (Fig. 8f and Supplementary Movie 17) illustrates the propagation in a normal heart, which is consistent with what was observed in the aforementioned canine case during normal sinus rhythm and the in silico case.

Supplementary video related to this article can be found at https://doi.org/10.1016/j.compbiomed.2019.103382.

3.7. In vivo EWI of a CRT patient during RV and BiV pacing

Noninvasive 4D electromechanical activation mapping of the ventricles using EWI was performed in an 84-year old male with CRT during RV and biventricular (BiV) pacing. The RV electrode was implanted in the apex while the LV electrode was in the coronary sinus. The electromechanical wave propagation was imaged using transthoracic high volume-rate ultrasound imaging during RV (Fig. 9a–e and Supplementary Movie 18) and BiV (Fig. 9g–k and Supplementary Movie 20) pacing. The EWI activation maps illustrate the activation pattern (Fig. 9f and Supplementary Movie 19 for RV pacing, Fig. 9l and Supplementary Movie 21 for BiV pacing). During RV pacing only, the earliest site of activation was found at the RV apex, which is consistent with the pacing electrode location. During BiV pacing, two sites of early activation were found: the RV apex and the antero-lateral region at the basal level. Both sites are consistent with the pacing electrodes location.

Supplementary video related to this article can be found at https://doi.org/10.1016/j.compbiomed.2019.103382.

4. Discussion

Cardiac arrhythmia and infarction are life-threatening diseases. Current methods used in the clinic to characterize cardiac arrhythmia are either not sufficiently spatially accurate, such as ECG, or invasive, superficial and time-consuming, such as electroanatomical mapping. A noninvasive 4D method to map cardiac activation of the full heart should prove pivotal in advancing the efficiency of cardiac disease diagnosis and treatment monitoring. 4D EWI is an imaging modality that not only can image the heart noninvasively, but also is radiation free and cost-effective [58].

In this proof-of-concept study, we show that the electromechanical activation of the entire heart can be mapped in 4D during a single cardiac cycle. In previous studies, EWI was performed with 2D ultrasound, and used different heartbeats for different imaging planes [19], which could render it inadequate for patients with inconsistent heartbeats and for imaging 3D propagation. Overcoming those limitations, 4D EWI is a robust method for noninvasive cardiac mapping. 4D EWI allows for identifying sites of early activation that may not be located in standard 2D echocardiographic planes. This is of key interest for accurately localizing arrhythmogenic sites that will be targeted for ablation and for assessing treatment. This technology could be used for arrhythmia diagnosis and treatment planning as well as patient follow-

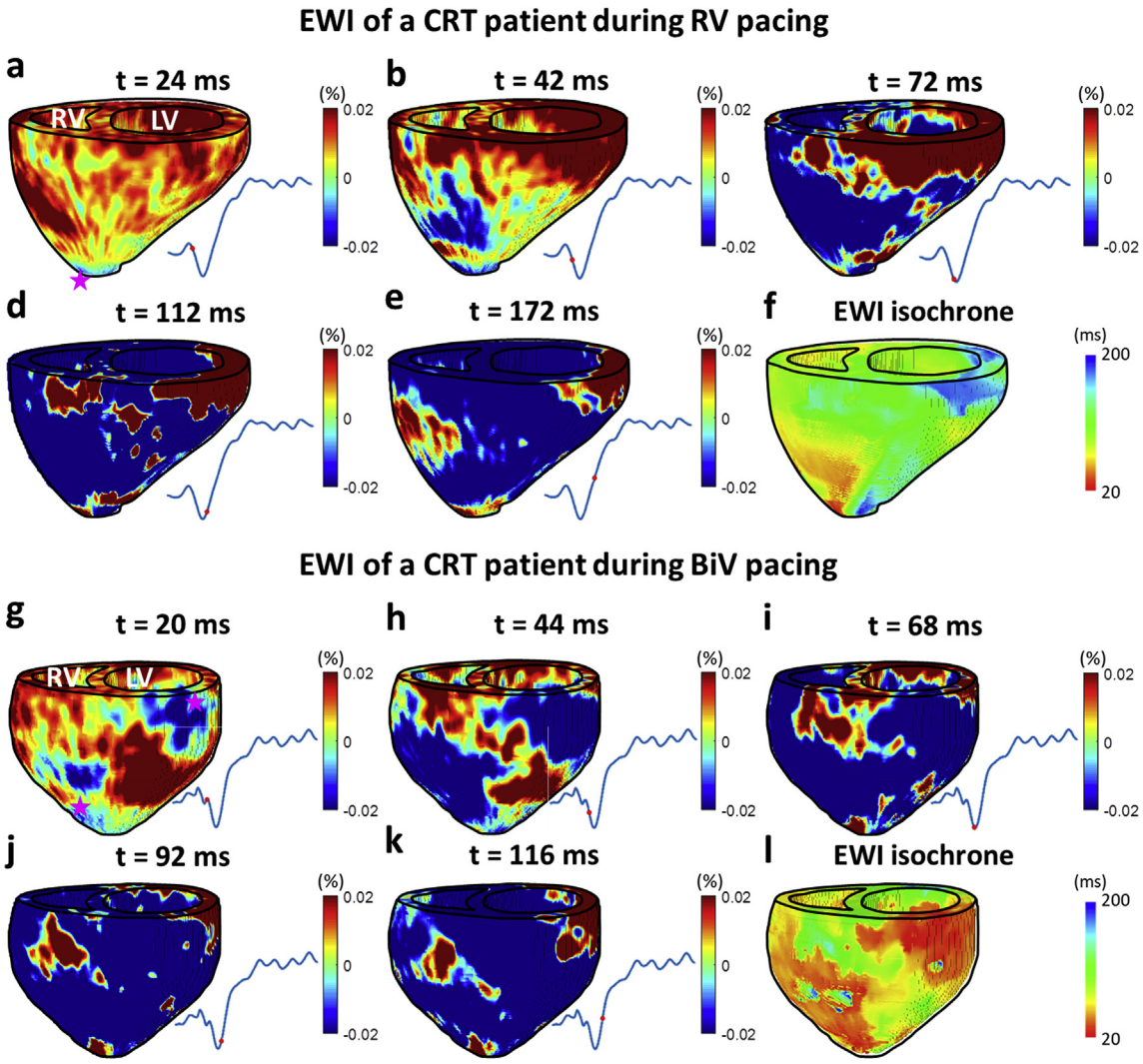

Fig. 9. In vivo electromechanical wave imaging of a cardiac resynchronization therapy (CRT) patient during right ventricular (RV) and biventricular (BiV) pacing. Snapshots of the axial strain obtained from 4D high volume-rate ultrasound imaging at different time points (a-e for RV pacing and g-k for BiV pacing) are shown. The ECG is also shown, with the corresponding time point indicated by a red dot. During RV pacing, the RV apex was activated first (a), while during BiV pacing, two regions of early activation were detected: the RV apex and the antero-lateral wall of the left ventricle (LV) at the basal level (g). The electromechanical activation times of the ventricles (f for RV pacing and l for BiV pacing) are consistent with the patient's pacing electrode locations (RV apex and coronary sinus). ★: earliest site of activation.

up at the point of care.

In this study, a new method was developed to semi-automatically detect the zero-crossing corresponding to the electromechanical activation time. This semi-automated method was compared to manual selection of zero-crossing and a good correlation was found. A constant amplitude threshold for the semi-automated method was used for a given activation map. This may not be always justified and can decrease the accuracy of activation time detection due to possible local inhomogeneity in mechanical properties of the myocardium, contraction magnitude and prestretch. An adaptive threshold method can be developed to account for mechanical and physiological inhomogeneity. Moreover, automatical selection of the onset of the QRS complex and of the P-wave can, in some cases, be challenging due to the presence of electrical noise.

4D EWI is performed with transthoracic echocardiography and therefore its implementation on a clinical ultrasound system would be seamless. It would require using diverging wave imaging as opposed to focused beams in order to image the full heart with a high volume-rate ($\geq$500 vol per second). The implementation of cardiac high volume-rate imaging in a clinical ultrasound system has been reported previously [59] while ultrasound data processing to obtain 3D electromechanical maps can be performed on-line. The integration of our methodology can be performed in existing clinical ultrasound scanners and provide an easily accessible imaging modality that can inform the cardiologist on the electromechanical function of the heart. By identifying early and late sites of activation as well as the activation pattern, pre-treatment planning can be improved and exposure time to ionizing radiation used to guide electrical mapping can be reduced. Our technique can complement invasive mapping methods such as electro-anatomical mapping and new non-invasive methods such as ECGi by providing new information, electromechanical activation, in a timely manner with simple, standard transthoracic echocardiogram. Our method can also be integrated into intracardiac and transesophageal echocardiography, to provide complementary information whenever the physician deems relevant to employ this modality.

The clinical application of this technique includes cardiac ablation treatment of arrhythmia and CRT optimization and monitoring for heart failure patients. So far, accurately locating arrhythmia in the clinic can only be performed invasively, using mapping catheters under fluoroscopic guidance in the clinic involving lengthy, ionizing

procedures. The use of 4D EWI would significantly decrease the procedure time as well as the risk of complications. In managing heart failure, up to 30%–50% of patients are reported to be non-responders to CRT [60] with CRT response strongly depending on lead placement [61], which is currently insufficiently guided. 4D EWI could also be used to optimize lead placement in CRT patients by monitoring the electromechanical activation of both ventricles simultaneously. Our in vivo findings presented herein are supported by computational modeling of a realistic electromechanical human heart model for both infarct-free and infarcted hearts, which has been shown to correctly predict the risk of sudden cardiac death in post-infarction patients [38,39]. Infarct tissue was modeled as electrically nonconductive and the infarct border zone size was marginal. This may not always truly represent the complex electrophysiological behavior of the border zone tissue. However, the main objective of the simulation study was to show the feasibility of performing 4D EWI using a 2D ultrasound array. Given the strong correlation obtained between finite-element and ultrasound simulation, we expect to observe the effect of changes in electromechanical modeling on ultrasound simulated EWI.

The electromechanical wave corresponds to the propagation of local myocardial shortening resulting from local electrical activation. As such, it is not a direct measurement of the electrical activity of the heart. There is a delay between the electrical and the electromechanical activation in the order of tens of milliseconds [14], referred as to the electromechanical delay, and usually increases from early to late sites of activations [33]. Therefore, EWI and electrical maps are not strictly equivocal. Given that it is not feasible to acquire transmural electrical activation throughout the heart in vivo, electromechanical activation maps can serve as a reliable surrogate for electrical activation times, simultaneously informing on both the mechanical and electrical activity of the heart.

In this study, a single diverging wave was used for volumetric imaging at high volume rates. This generates images with decreased contrast and resolution compared to conventionally focused imaging and may lead to suboptimal strain estimates and to local inaccuracies in the activation pattern, that can be observed in both normal and paced rhythms. Previous studies have shown that coherent compounding of diverging waves can provide high contrast and resolution while maintaining high volume-rate imaging [53]. In addition, the 2D array used in this study has an active aperture of 9.6 mm, which is more than twice smaller than the aperture (20.5 mm) of the 1D array (P4-2, ATL) used in previous 2D EWI studies [13]. This also contributes to a decrease in image resolution compared to 2D imaging. A lateral point spread function of 5.8 mm for the two systems with multiplexer, of 5.6 mm for the four systems without multiplexer and of 3.7 mm for the P4-2 1D array, at a depth of 40 mm was found. Despite the relatively good agreement found between 4D EWI and electroanatomical mapping in this preliminary study, our technique can be improved with the use of coherent compounding and a larger 2D array. In addition, our upgraded 3D ultrasound system, using four synchronized ultrasound scanners instead of two with a multiplexer, would provide better imaging quality, by allowing additional compounded waves. At an imaging depth of 16 cm, up to nine diverging waves can be used with a compounded frame rate of 500 volumes per second without multiplexing.

Another limitation of the current study is that the co-registration between experimental electrical and EWI maps was performed manually albeit using anatomical landmarks. The operator had knowledge of both activation maps during the co-registration process. The correlation coefficient obtained in this study is on the same order of magnitude of those obtained in previous studies using 2D EWI [13,19,20]. In the case of RV pacing, the slope of the linear regression between EWI and electrical activation times was equal to 0.9, which was underestimated since the electromechanical delay is expected to increase from early to late activated regions [62,63]. This can be due to imperfect co-registration between both activation maps and to poorer estimation of strain and activation times owing to lower image quality using single diverging wave imaging as aforementioned. While some local discrepancies, such as in the lateral LV wall during apical pacing (Fig. 6g and h), can be found between the EWI and the electrical maps, due to poorer sonographic contrast or to imperfect co-registration, the general EWI and electrical activation pattern was similar. These experimental findings were supported by our simulation study showing that 4D EWI can be visualized and indicated good agreement between electrical and electromechanical activation maps in the ventricles. Mechanical simulation of the atria could not be carried out due to the limited resolution of MRI to accurately image atrial thin wall and complex pattern of fibers.

Although, all four chambers can be mapped with 4D EWI simultaneously (Figs. 5 and 8), in some cases we imaged only a single (Fig. 7) or both (Figs. 6 and 9) ventricles, since these were the regions of interest (ventricular pacing and validation against electrical mapping of the ventricles). In these cases, the other chambers were not necessarily in view or could not be clearly delineated due to poor contrast since the sonographer was attempting to best image the region of interest. Similarly, while the noninvasive aspect of 4D EWI was demonstrated in humans in this study, open-chest canine experiments were also performed, in order to pace epicardially and validate our EWI measurements against electrical mapping without the use of fluoroscopy.

Although, the imaging sequence used here has reduced spatial resolution due to unfocused wave emission and which can affect EWI map quality, excellent agreement was obtained between the ultrasound and finite-element simulations. Other potential sources of noise in EWI can be due to in vivo conditions such as ultrasound attenuation, clutter noise and echocardiographic window quality. In addition, the quality of images obtained in the open-chest canine in vivo was higher than in the humans in vivo since there was no attenuation from fat tissue and no artifacts from the rib cage, in particular. Nevertheless, the ultrasound acquisitions in normal human hearts and in the CRT patient indicate the feasibility of 4D EWI in humans noninvasively.

5. Conclusion

This is a proof-of-concept study demonstrating that noninvasive imaging of the 4D electromechanical activation of the heart in a single heartbeat is feasible in vivo including in a heart disease patient. Future studies will focus on improving image quality, full automation and validation in a larger number of subjects. This technology could be employed as a routine tool for screening as well as for diagnosis and therapy guidance for heart disease patients at the point of care.

Author contribution

J.G. and E.E.K. designed research and wrote the paper; D.W. and N.T. designed and conducted the finite-element simulations and contributed to the Methods text; J.G. performed the ultrasound simulations, designed the experiment and processed the data; C.S.G. coordinated the patient study, performed the ultrasound scans and electroanatomical mapping. All authors read and approved the manuscript.

Conflicts of interest

None Declared.

Acknowledgments

This work was supported in part by the National Institutes of Health, United States (R01-EB006042, R01-HL114358, R01HL140646 and R01-HL126802), the Leducq Foundation, France and the NIH Director's Pioneer Award, United States (PD1HL123271). The authors would like to thank Vincent Sayseng, MS and Lea Melki, MS for their assistance during the canine experiments, Rachel Weber, RDCS, RVT for the

ultrasound scans and Hasan Garan, MD for his assistance.

Appendix A. Supplementary data

Supplementary data to this article can be found online at https://doi.org/10.1016/j.compbiomed.2019.103382.

References

[1] E.J. Benjamin, et al., Heart disease and stroke statistics-2018 update: a report from the American heart association, Circulation 137 (2018) e67–e492, https://doi.org/10.1161/cir.0000000000000558.

[2] F. Rahman, G.F. Kwan, E.J. Benjamin, Global epidemiology of atrial fibrillation, Nat. Rev. Cardiol. 11 (2014) 639–654, https://doi.org/10.1038/nrcardio.2014.118.

[3] G.A. Roth, et al., Global, regional, and national burden of cardiovascular diseases for 10 causes, 1990 to 2015, J. Am. Coll. Cardiol. 70 (2017) 1–25 https://doi.org/10.1016/j.jacc.2017.04.052.

[4] D.J. Gladstone, et al., Atrial fibrillation in patients with cryptogenic stroke, N. Engl. J. Med. 370 (2014) 2467–2477, https://doi.org/10.1056/NEJMoa1311376.

[5] H.J. Lin, et al., Stroke severity in atrial fibrillation. The Framingham Study, Stroke 27 (1996) 1760–1764.

[6] A. Eisen, et al., Sudden cardiac death in patients with atrial fibrillation: insights from the ENGAGE AF-TIMI 48 trial, J. American. Heart. Assoc. 5 (2016).

[7] G.F. Tomaselli, D.P. Zipes, What causes sudden death in heart failure? Circ. Res. 95 (2004) 754.

[8] S. Nattel, Decade in review–arrhythmias: cardiac fibrillation–challenges and evolving solutions, Nat. Rev. Cardiol. 11 (2014) 626–627, https://doi.org/10.1038/nrcardio.2014.133.

[9] C. Knackstedt, P. Schauerte, P. Kirchhof, Electro-anatomic mapping systems in arrhythmias, Europace 10 (Suppl 3) (2008) iii28–34, https://doi.org/10.1093/europace/eun225.

[10] C. Ramanathan, R.N. Ghanem, P. Jia, K. Ryu, Y. Rudy, Noninvasive electrocardiographic imaging for cardiac electrophysiology and arrhythmia, Nat. Med. 10 (2004) 422–428, https://doi.org/10.1038/nm1011.

[11] Y. Wang, et al., Noninvasive electroanatomic mapping of human ventricular arrhythmias with electrocardiographic imaging, Sci. Transl. Med. 3 (2011) 98ra84.

[12] J. Provost, W.N. Lee, K. Fujikura, E.E. Konofagou, Electromechanical wave imaging of normal and ischemic hearts in vivo, IEEE Trans. Med. Imaging 29 (2010) 625–635, https://doi.org/10.1109/tmi.2009.2030186.

[13] J. Provost, W.-N. Lee, K. Fujikura, E.E. Konofagou, Imaging the electromechanical activity of the heart in vivo, Proc. Natl. Acad. Sci. 108 (2011) 8565–8570, https://doi.org/10.1073/pnas.1011688108.

[14] J.M. Cordeiro, L. Greene, C. Heilmann, D. Antzelevitch, C. Antzelevitch, Transmural heterogeneity of calcium activity and mechanical function in the canine left ventricle, Am. J. Physiol. Heart Circ. Physiol. 286 (2004) H1471–H1479, https://doi.org/10.1152/ajpheart.00748.2003.

[15] H. Kanai, Y. Koiwa, Myocardial rapid velocity distribution, Ultrasound Med. Biol. 27 (2001) 481–498.

[16] M. Pernot, K. Fujikura, S.D. Fung-Kee-Fung, E.E. Konofagou, ECG-gated, mechanical and electromechanical wave imaging of cardiovascular tissues in vivo, Ultrasound Med. Biol. 33 (2007) 1075–1085, https://doi.org/10.1016/j.ultrasmedbio.2007.02.003.

[17] H.J. Vos, et al., Cardiac shear wave velocity detection in the porcine heart, Ultrasound Med. Biol. 43 (2017) 753–764, https://doi.org/10.1016/j.ultrasmedbio.2016.11.015.

[18] E.W. Remme, et al., Mechanisms of preejection and postejection velocity spikes in left ventricular myocardium: interaction between wall deformation and valve events, Circulation 118 (2008) 373–380, https://doi.org/10.1161/circulationaha.107.748491.

[19] A. Costet, et al., Electromechanical wave imaging (EWI) validation in all four cardiac chambers with 3D electroanatomic mapping in canines in vivo, Phys. Med. Biol. 61 (2016) 8105–8119, https://doi.org/10.1088/0031-9155/61/22/8105.

[20] J. Grondin, et al., Validation of electromechanical wave imaging in a canine model during pacing and sinus rhythm, Heart Rhythm 13 (2016) 2221–2227, https://doi.org/10.1016/j.hrthm.2016.08.010.

[21] J. Provost, V. Gurev, N. Trayanova, E.E. Konofagou, Mapping of cardiac electrical activation with electromechanical wave imaging: an in silico-in vivo reciprocity study, Heart Rhythm 8 (2011) 752–759, https://doi.org/10.1016/j.hrthm.2010.12.034.

[22] E. Bunting, et al., Imaging the propagation of the electromechanical wave in heart failure patients with cardiac resynchronization therapy, Pacing Clin. Electrophysiol. 40 (2017) 35–45, https://doi.org/10.1111/pace.12964.

[23] L. Melki, et al., Localization of accessory pathways in pediatric patients with Wolff-Parkinson-white syndrome using 3d-rendered electromechanical wave imaging, JACC Clin Electrophysiol 5 (2019) 427–437, https://doi.org/10.1016/j.jacep.2018.12.001.

[24] J. Christoph, et al., Electromechanical vortex filaments during cardiac fibrillation, Nature 555 (2018) 667–672, https://doi.org/10.1038/nature26001.

[25] K.H. ten Tusscher, D. Noble, P.J. Noble, A.V. Panfilov, A model for human ventricular tissue, Am. J. Physiol. Heart Circ. Physiol. 286 (2004) H1573–H1589, https://doi.org/10.1152/ajpheart.00794.2003.

[26] J.J. Rice, F. Wang, D.M. Bers, P.P. de Tombe, Approximate model of cooperative activation and crossbridge cycling in cardiac muscle using ordinary differential equations, Biophys. J. 95 (2008) 2368–2390, https://doi.org/10.1529/biophysj.107.119487.

[27] Y. Hu, V. Gurev, J. Constantino, J.D. Bayer, N.A. Trayanova, Effects of mechano-electric feedback on scroll wave stability in human ventricular fibrillation, PLoS One 8 (2013) e60287, , https://doi.org/10.1371/journal.pone.0060287.

[28] J. Constantino, Y. Hu, A.C. Lardo, N.A. Trayanova, Mechanistic insight into prolonged electromechanical delay in dyssynchronous heart failure: a computational study, Am. J. Physiol. Heart Circ. Physiol. 305 (2013) H1265–H1273, https://doi.org/10.1152/ajpheart.00426.2013.

[29] V. Gurev, T. Lee, J. Constantino, H. Arevalo, N.A. Trayanova, Models of cardiac electromechanics based on individual hearts imaging data: image-based electromechanical models of the heart, Biomechanics Model. Mechanobiol. 10 (2011) 295–306, https://doi.org/10.1007/s10237-010-0235-5.

[30] X. Jie, V. Gurev, N. Trayanova, Mechanisms of mechanically induced spontaneous arrhythmias in acute regional ischemia, Circ. Res. 106 (2010) 185–192, https://doi.org/10.1161/circresaha.109.210864.

[31] N.A. Trayanova, J. Constantino, V. Gurev, Electromechanical models of the ventricles, Am. J. Physiol. Heart Circ. Physiol. 301 (2011) H279–H286, https://doi.org/10.1152/ajpheart.00324.2011.

[32] S. Land, et al., Verification of cardiac mechanics software: benchmark problems and solutions for testing active and passive material behaviour, Proc Math Phys Eng Sci 471 (2015) 20150641, https://doi.org/10.1098/rspa.2015.0641.

[33] V. Gurev, J. Constantino, J.J. Rice, N.A. Trayanova, Distribution of electromechanical delay in the heart: insights from a three-dimensional electromechanical model, Biophys. J. 99 (2010) 745–754, https://doi.org/10.1016/j.bpj.2010.05.028.

[34] V. Gurev, et al., Mechanisms underlying isovolumic contraction and ejection peaks in seismocardiogram morphology, J. Med. Biol. Eng. 32 (2012) 103–110.

[35] Y. Hu, V. Gurev, J. Constantino, N. Trayanova, Efficient preloading of the ventricles by a properly timed atrial contraction underlies stroke work improvement in the acute response to cardiac resynchronization therapy, Heart Rhythm 10 (2013) 1800–1806, https://doi.org/10.1016/j.hrthm.2013.08.003.

[36] Y. Hu, V. Gurev, J. Constantino, N. Trayanova, Optimizing cardiac resynchronization therapy to minimize ATP consumption heterogeneity throughout the left ventricle: a simulation analysis using a canine heart failure model, Heart Rhythm 11 (2014) 1063–1069, https://doi.org/10.1016/j.hrthm.2014.03.021.

[37] K.M. Lim, et al., Comparison of the effects of continuous and pulsatile left ventricular-assist devices on ventricular unloading using a cardiac electromechanics model, J. Physiol. Sci. 62 (2012) 11–19, https://doi.org/10.1007/s12576-011-0180-9.

[38] H.J. Arevalo, et al., Arrhythmia risk stratification of patients after myocardial infarction using personalized heart models, Nat. Commun. 7 (2016) 11437, https://doi.org/10.1038/ncomms11437.

[39] A. Prakosa, et al., Personalized virtual-heart technology for guiding the ablation of infarct-related ventricular tachycardia, Nature Biomedical Engineering (2018), https://doi.org/10.1038/s41551-018-0282-2.

[40] J.D. Bayer, R.C. Blake, G. Plank, N.A. Trayanova, A novel rule-based algorithm for assigning myocardial fiber orientation to computational heart models, Ann. Biomed. Eng. 40 (2012) 2243–2254, https://doi.org/10.1007/s10439-012-0593-5.

[41] A. Prakosa, et al., Methodology for image-based reconstruction of ventricular geometry for patient-specific modeling of cardiac electrophysiology, Prog. Biophys. Mol. Biol. 115 (2014) 226–234, https://doi.org/10.1016/j.pbiomolbio.2014.08.009.

[42] http://www.field-ii.dk/.

[43] J.A. Jensen, Simulation of advanced ultrasound systems using Field II, 2nd IEEE International Symposium on Biomedical Imaging: Nano to Macro (IEEE Cat No. 04EX821) 631 (2004) 636–639, https://doi.org/10.1109/isbi.2004.1398618.

[44] J.A. Jensen, N.B. Svendsen, Calculation of pressure fields from arbitrarily shaped, apodized, and excited ultrasound transducers, IEEE Trans. Ultrason. Ferroelectr. Freq. Control 39 (1992) 262–267, https://doi.org/10.1109/58.139123.

[45] G.E. Tupholme, Generation of acoustic pulses by baffled plane pistons, Mathematika 16 (1969) 209–224, https://doi.org/10.1112/s0025579300008184.

[46] P.R. Stepanishen, The time-dependent force and radiation impedance on a piston in a rigid infinite planar baffle, J. Acoust. Soc. Am. 49 (1971) 841–849, https://doi.org/10.1121/1.1912424.

[47] J. Grondin, V. Sayseng, E.E. Konofagou, Cardiac strain imaging with coherent compounding of diverging waves, IEEE Trans. Ultrason. Ferroelectr. Freq. Control 64 (2017) 1212–1222, https://doi.org/10.1109/tuffc.2017.2717792.

[48] S. Fekkes, et al., 2-D versus 3-D cross-correlation-based radial and circumferential strain estimation using multiplane 2-D ultrafast ultrasound in a 3-D atherosclerotic carotid artery model, IEEE Trans. Ultrason. Ferroelectr. Freq. Control 63 (2016) 1543–1553, https://doi.org/10.1109/tuffc.2016.2603189.

[49] Y. Wang, E. Helminen, Jiang, J. Building a virtual simulation platform for quasi-static breast ultrasound elastography using open source software: a preliminary investigation, Med. Phys. 42 (2015) 5453–5466, https://doi.org/10.1118/1.4928707.

[50] A. Ramalli, E. Boni, A.S. Savoia, P. Tortoli, Density-tapered spiral arrays for ultrasound 3-D imaging, IEEE Trans. Ultrason. Ferroelectr. Freq. Control 62 (2015) 1580–1588, https://doi.org/10.1109/tuffc.2015.007035.

[51] S. Bayat, et al., Investigation of physical phenomena underlying temporal-enhanced ultrasound as a new diagnostic imaging technique: theory and simulations, IEEE Trans. Ultrason. Ferroelectr. Freq. Control 65 (2018) 400–410, https://doi.org/10.1109/tuffc.2017.2785230.

[52] H. Hasegawa, H. Kanai, High-frame-rate echocardiography using diverging transmit beams and parallel receive beamforming, J. Med. Ultrason. 38 (2001) 129–140, https://doi.org/10.1007/s10396-011-0304-0 2011.

[53] J. Provost, et al., 3D ultrafast ultrasound imaging in vivo, Phys. Med. Biol. 59

(2014) L1–L13, https://doi.org/10.1088/0031-9155/59/19/l1.
[54] A.S. Harris, Delayed development of ventricular ectopic rhythms following experimental coronary occlusion, Circulation 1 (1950) 1318–1328.
[55] J. Luo, E. Konofagou, A fast normalized cross-correlation calculation method for motion estimation, IEEE Trans. Ultrason. Ferroelectr. Freq. Control 57 (2010) 1347–1357, https://doi.org/10.1109/tuffc.2010.1554.
[56] J. Luo, J. Bai, P. He, K. Ying, Axial strain calculation using a low-pass digital differentiator in ultrasound elastography, IEEE Trans. Ultrason. Ferroelectr. Freq. Control 51 (2004) 1119–1127.
[57] E. Cingolani, J.I. Goldhaber, E. Marban, Next-generation pacemakers: from small devices to biological pacemakers, Nat. Rev. Cardiol. (2017), https://doi.org/10.1038/nrcardio.2017.165.
[58] J. Hung, et al., 3D echocardiography: a review of the current status and future directions, J. Am. Soc. Echocardiogr. 20 (2007) 213–233, https://doi.org/10.1016/j.echo.2007.01.010.
[59] P. Santos, G.U. Haugen, L. Løvstakken, E. Samset, J. D'hooge, Diverging wave volumetric imaging using subaperture beamforming, IEEE Trans. Ultrason. Ferroelectr. Freq. Control 63 (2016) 2114–2124, https://doi.org/10.1109/tuffc.2016.2616172.
[60] J.C. Daubert, et al., EHRA/HRS expert consensus statement on cardiac resynchronization therapy in heart failure: implant and follow-up recommendations and management, Heart Rhythm 9 (2012) 1524–1576, https://doi.org/10.1016/j.hrthm.2012.07.025 2012.
[61] C. Ypenburg, et al., Optimal left ventricular lead position predicts reverse remodeling and survival after cardiac resynchronization therapy, J. Am. Coll. Cardiol. 52 (2008) 1402–1409, https://doi.org/10.1016/j.jacc.2008.06.046.
[62] F.R. Badke, P. Boinay, J.W. Covell, Effects of ventricular pacing on regional left ventricular performance in the dog, Am. J. Physiol. 238 (1980) H858–H867, https://doi.org/10.1152/ajpheart.1980.238.6.H858.
[63] F.W. Prinzen, et al., The time sequence of electrical and mechanical activation during spontaneous beating and ectopic stimulation, Eur. Heart J. 13 (1992) 535–543.